Interaction of an unconfined vortex with a solid surface

L. Parras and R. Fernandez-Feria
Universidad de Málaga, E.T.S. Ingenieros Industriales, 29013 Málaga, Spain

(Received 29 January 2007; accepted 13 April 2007; published online 19 June 2007)

The interaction of an open vortex with a solid plane perpendicular to the axis of the vortex is analyzed numerically. We solve the axisymmetric, incompressible Navier-Stokes equations with boundary conditions that far from the axis correspond to the near-inviscid far-field of Long's similarity solution for an open vortex. Continuation techniques are used to solve the equations of motion for varying Reynolds numbers. When this parameter is large enough, a vortex breakdown phenomenon occurs, producing a small region of reversed flow at the axis. This region increases in size and migrates toward the solid plane for increasing Reynolds numbers. The subsequent intensification of the swirl near both the axis and the surface generates a bifurcation with nonuniqueness of the solution corresponding to a new, more intense, vortex breakdown. At the end, for Reynolds numbers above a critical value, the flow acquires a two-celled structure, with a region of reversed flow all along the axis surrounded by an annular updraft region with intensified swirl. For large Reynolds numbers this flow structure tends, far above from the plane, to Long's self-similar solution of Type II. Thus, we show that of the two different similarity solutions for high Reynolds numbers found by Long for a given flow force, only that with negative axial velocity at the axis (Type II solution) is compatible with the viscous interaction of the vortex with a solid surface. We also find that the corresponding flow force increases linearly with the Reynolds number, so that the solution tends for large Reynolds numbers to the similarity solution with the most negative axial velocity at the axis. This transition from one-cell to two-cell flow configuration, and its relation to the intensification of the swirl in the flow, is in agreement with observations of intense tornado-like vortices, where the flow at the axis is directed downward, while the rotation of the flow is intensified in an annular updraft. © *2007 American Institute of Physics*.
[DOI: 10.1063/1.2737783]

I. INTRODUCTION

The viscous interaction of a vortex with a solid plane perpendicular to its axis is a problem of industrial and atmospheric interest. This interaction may be so strong as to affect the global structure of the original vortex, even far away from the surface. A significative example, though not a vortex in the usual sense, is the rotating flow with constant angular velocity (solid body rotation) above a solid plane. This interaction was first studied by Bodewadt,[1] finding one of the few exact solutions to the full Navier-Stokes equations. The original, purely rotating flow is completely transformed by the interaction with the solid surface, producing a radial inflow near the plane and an axial upward flow that extends up indefinitely far from the plane.[1,2]

For high Reynolds numbers, the boundary layer structure close to the plane has been analyzed for several types of nearly inviscid vortices.[3–8] However, these boundary layer solutions are not valid near the axis, where the flow turns upward to form the viscous core of the vortex, thus failing to uncover the main feature of the vortex-surface interaction. For this reason, we have performed here a series of numerical simulations, using the full incompressible Navier-Stokes equations, to analyze the interaction of a relevant type of vortex with a solid surface. In particular, we have selected a family of vortices that far from the axis and far from the plane (located at $z=0$) corresponds, for high Reynolds numbers, to the outer inviscid behavior of Long's vortex.[9] That is to say, we consider a family of vortices whose velocity field $\mathbf{v}\equiv(u,v,w)$ in cylindrical polar coordinates (r,θ,z), for large r and z, behaves as

$$u\sim 0, \quad v\sim L\frac{W_o}{r}, \quad w\sim \frac{W_o}{r}, \tag{1}$$

where W_o is a constant with the dimensions of a circulation and L is the nondimensional swirl parameter. We have selected this vortex instead of a potential vortex with just circumferential velocity because most of actual vortices of interest have also a significant meridional motion even far away from the axis. In fact, the flow (1) is the large r and large z behavior of an exact solution to Euler equations, which can be written as

$$\mathbf{v}=\mathbf{V}(y)\frac{1}{r}, \quad y\equiv\frac{r}{z}, \tag{2}$$

where the three components of the vector function $\mathbf{V}(y)$ can be obtained from the integration of just one ordinary differential equation.[10] This solution is the particular case $m=1$ of a more general family of inviscid vortices with a radial decay of the form r^{m-2} in (2). It is singular both at the axis $(y=0)$ and at the solid surface $(y\to\infty)$. At the axis it is regularized by a viscous slender region with self-similar structure, which constitutes the so-called Long's vortex,[9,11] while at the solid

plane it is regularized by a viscous boundary layer, which has also a self-similar structure, but now of the second kind.[8] However, neither of these boundary layers is valid near the origin $(r=0,z=0)$, where the vortex axis intersects the plane, and where the flow structure cannot be described by a boundary layer approximation. In that region, the radial inflow in the boundary layer turns upward to form the viscous core of the vortex, which, sufficiently far from the surface, and for sufficiently high Reynolds numbers, *has to* tend to one member of the family of Long's self-similar solutions. One of the main objectives of this paper is to find out which one of these self-similar solutions corresponds to a free vortex interacting with a solid plane. Also, we want to describe how this solution is reached as the Reynolds number is increased. To that end we solve numerically the full incompressible and axisymmetric Navier-Stokes equations with boundary conditions far from the axis given by the composite solution constituted by the inviscid solution (2) for large r (large y) plus the self-similar boundary layer solution near the plane.[8]

Burggraf and Foster[12] made a somewhat related analysis some time ago, but they used the parabolic, or near-axis, approximation of the Navier-Stokes equations for large Reynolds numbers, which, of course, cannot model the interaction of the vortex with a solid surface. These authors integrated the parabolic equation starting from arbitrary vortices decaying as r^{-1} at a given axial location, and followed their parabolic evolution as z increased. They found that the downstream solution either breaks down or tends to Long's self-similar solution of Type II (i.e., with negative axial velocity at the axis, see below) as $z\to\infty$, depending on the parameters of the initial vortex. A similar conclusion was recently found by Perez-Saborid *et al.*,[13] also using the parabolic approximation of the flow equations, including the energy equation. As a substantial difference, here we use the full Navier-Sokes equations and consider a problem of great practical interest, the interaction of a free vortex with a solid surface. We also find that the solution for large z tends to Type II Long's self-similar solution if the Reynolds number is large enough, but we connect the formation of this two-celled structure with the swirl intensification occurring in tornado-like vortices interacting with a solid surface. As we shall see, the flow structure in the region near the axis where the vortex meets the wall is quite complex, with vortex breakdown and other flow transitions taking place as the Reynolds number increases. Similar complex structures, but for external far-field vortices which do not match the one considered in this work as a boundary condition, have been observed experimentally and discussed by Phillips and Khoo,[14,15] and by Hirsa, Lopez, and Kim.[16] In particular, these latter authors found that the essential dynamics in the effusive corner region are axisymmetric, with a large toroidal structure developing from the wall boundary layer. However, in the work of Phillips and Khoo, the appearance of the near-axis structure is related to vortex breakdown. In our numerical simulations, we find an interplay between both mechanisms, vortex breakdown at the axis, and effusing boundary layer flow at the wall, which at the end, for sufficiently high Reynolds numbers, tends to the formation of a two-celled flow structure far from the wall. This two-celled structure corresponds, as we shall show, to a Type II Long's vortex. It has no relation to Sullivan's two-cell vortex.[17] Sullivan's exact solution to the Navier-Stokes equations, which does not satisfy the no-slip boundary condition at the solid wall $z=0$, has a radial structure of the tangential velocity qualitatively similar to Long's Type II vortex. However, this tangential velocity has no axial variation like in Long's vortex, and, what is more relevant here, the axial velocity in Sullivan's vortex is completely different: it grows with the axial distance z and tends to a constant far from the axis, while the axial velocity in Long's vortex decays as r^{-1} far from the axis [Eq. (2)] and presents a more complex axial variation, which, for instance, behaves as $1/z$ at the axis.[9,11]

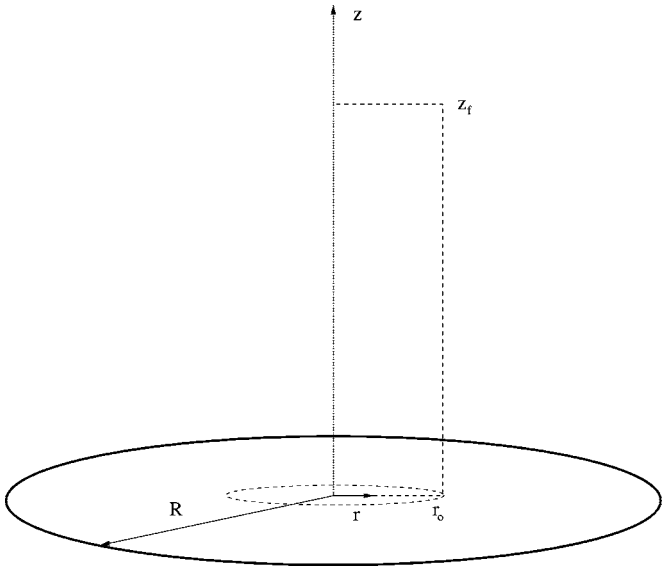

FIG. 1. Sketch of the *dimensional* integration domain and coordinates.

II. FORMULATION OF THE PROBLEM AND NUMERICAL METHOD

A. Mathematical formulation

We consider here the incompressible and axisymmetric flow in a domain above a solid plane at $z=0$, and inside a cylindrical region of radius r_0 and height z_f (see Fig. 1): The swirling flow enters through the lateral surface $r=r_0$, and goes out through the upper surface, $z=z_f\gg r_0$. To avoid boundary conditions for the pressure, we use a formulation of the flow equations in terms of the stream function, the circulation, and the azimuthal component of the vorticity, commonly used in this type of flow (e.g., Ref. 18). First we define the following dimensionless variables:

$$r^*\equiv\frac{r}{r_0},\quad z^*\equiv\frac{z}{z_0}, \tag{3}$$

where z_0 is an arbitrary characteristic axial length such that

$$\Delta\equiv\frac{r_0}{z_0}\ll 1; \tag{4}$$

$$\Psi^* \equiv \frac{\Psi}{V_0 r_0^2}, \quad \Gamma^* \equiv \frac{\Gamma}{V_0 r_0}, \quad \Pi^* \equiv \frac{r\eta}{V_0}, \tag{5}$$

where V_0 is a characteristic velocity that will be taken from (1) as $V_0 = W_0/r_0$, and the stream function Ψ, the circulation Γ, and the azimuthal component of the vorticity η are defined in terms of the velocity field (u,v,w) as

$$u = -\frac{1}{r}\frac{\partial \Psi}{\partial z}, \quad w = \frac{1}{r}\frac{\partial \Psi}{\partial r}, \quad \Gamma = rv, \tag{6}$$

$$\eta = \frac{\partial u}{\partial z} - \frac{\partial w}{\partial r}. \tag{7}$$

With this formulation, the continuity equation is satisfied identically, and the equations to be solved are the azimuthal component of the vorticity equation for the evolution of Π^*, the azimuthal component of the momentum equation for Γ^*, and the definition (7) of the vorticity in terms of the stream function (6) for Ψ^*. In dimensionless form, they can be written as[18] (in what follows, we shall drop the superscript * in the dimensionless variables, understanding that all variables are dimensionless, except otherwise specified)

$$\frac{\partial \Pi}{\partial t} - \frac{1}{r}\frac{\partial \Psi}{\partial z}\frac{\partial \Pi}{\partial r} + \frac{1}{r}\frac{\partial \Psi}{\partial r}\frac{\partial \Pi}{\partial z} + \frac{2\Pi}{r^2}\frac{\partial \Psi}{\partial z} = \frac{2\Gamma}{r^2}\frac{\partial \Gamma}{\partial z} + \frac{1}{\mathrm{Re}\,\Delta}\nabla_*^2 \Pi, \tag{8}$$

$$\frac{\partial \Gamma}{\partial t} - \frac{1}{r}\frac{\partial \Psi}{\partial z}\frac{\partial \Gamma}{\partial r} + \frac{1}{r}\frac{\partial \Psi}{\partial r}\frac{\partial \Gamma}{\partial z} = \frac{1}{\mathrm{Re}\,\Delta}\nabla_*^2 \Gamma, \tag{9}$$

$$\Pi = -\nabla_*^2 \Psi, \tag{10}$$

where

$$\nabla_*^2 \equiv \Delta^2 \frac{\partial^2}{\partial z^2} + \frac{\partial^2}{\partial r^2} - \frac{1}{r}\frac{\partial}{\partial r} \tag{11}$$

and

$$\mathrm{Re} = \frac{V_0 r_0}{\nu} = \frac{W_0}{\nu} \tag{12}$$

is the Reynolds number, with ν the kinematic viscosity.

The main input of the problem solved here is the boundary condition at $r=1$ ($r=r_0$ in terms of the dimensional radius), which is given by the composite solution of an inviscid flow of the form (2) and the corresponding matching with its viscous boundary layer near $z=0$. This boundary layer solution was found in Ref. 8 to be a similarity solution of the *second kind,* which contains an additional, and arbitrary, radial length R (see Fig. 1). Therefore, without loss of generality (since R is arbitrary), we assume that r_0 is much smaller than R, but of course much larger than the boundary layer thickness. Thus, the boundary condition at $r=1$ can be written as the following composite expressions:

$$\Psi(r=1,z) \equiv \Psi_1(z) = \Psi_{\mathrm{in}} + \Psi_{\mathrm{bl}} - \Psi_{\mathrm{comm}}, \tag{13}$$

$$\Gamma(r=1,z) \equiv \Gamma_1(z) = \Gamma_{\mathrm{in}} + \Gamma_{\mathrm{bl}} - \Psi_{\mathrm{comm}}, \tag{14}$$

$$\Pi(r=1,z) \equiv \Pi_1(z) = \Pi_{\mathrm{in}} + \Pi_{\mathrm{bl}} - \Pi_{\mathrm{comm}}, \tag{15}$$

where the subscripts in, bl, and comm make reference to the inviscid solution, the boundary layer solution, and the common part, respectively. Each of these solutions will be briefly described next.

In the formulation $\Psi-\Gamma-\Pi$, the inviscid flow (2) can be written as

$$\Psi_{\mathrm{in}} = LrY(y), \quad \Gamma_{\mathrm{in}} = L, \quad \Pi_{\mathrm{in}} = -\nabla_*^2 \Psi_{\mathrm{in}}, \tag{16}$$

where in the present dimensionless variables $y = \Delta r/z$, and the function $Y(y)$ comes from the solution to an ordinary differential equation.[10] For the case (2) considered here of a flow decaying as r^{-1} ($m=1$ in the notation of Refs. 10 and 11, corresponding to Long's vortex), this function can be obtained analytically:[10]

$$Y(y) = \frac{\sqrt{2}}{L}\frac{(\sqrt{1+y^2}-1)^{1/2}}{y}. \tag{17}$$

In addition, as is observed in (16), the inviscid circulation in this case is just a constant, which in the dimensionless variable Γ is equal to the swirl parameter L. As shown in Ref. 11, the only value of L for which this inviscid solution can be regularized at the axis by viscosity (in the present case with $m=1$) is $L=\sqrt{2}$, so that this will be the only value of the swirl parameter considered in what follows. This coupling between meridional and azimuthal velocity through $L=\sqrt{2}$ is implicit in Long's vortex.[9,12]

The boundary layer solution near the solid plane at $z=0$, assuming that $r_0 \ll R$, can be written as[8]

$$\Psi_{\mathrm{bl}} = (\mathrm{Re}_0/2)^{-1/3} f(\gamma), \quad \Gamma_{\mathrm{bl}} = \sqrt{2} g(\gamma), \quad \Pi_{\mathrm{bl}} = -\nabla_*^2 \Psi_{\mathrm{bl}}. \tag{18}$$

In these expressions, the functions $f(\gamma)$ and $g(\gamma)$, where

$$\gamma \equiv 2^{1/3}\mathrm{Re}_0^{2/3}\frac{rz}{\Delta}, \quad \mathrm{Re}_0 \equiv \mathrm{Re}\Delta, \tag{19}$$

are the solution to a couple of ordinary differential equations,[8]

$$f''' + ff'' + f'^2 = 0, \quad g'' + f'g' = 0, \tag{20}$$

$$f(0) = f'(0) = g(0) = 0, \quad f(\gamma \to \infty) \to \sqrt{\gamma}, \quad g(\gamma \to \infty) \to L/\sqrt{2}, \tag{21}$$

with primes denoting differentiation with respect to γ. In writing Eqs. (18) and (19), we have also assumed that

$$\left(\frac{r_0}{R}\right)^3 = \Delta \equiv \frac{r_0}{z_0} \ll 1. \tag{22}$$

This choice of the characteristic axial length z_0 allows us to eliminate the arbitrary length R in the formulation of the problem, without loss of generality. Thus, the only two dimensionless parameters in the problem are $\mathrm{Re}_0[=\mathrm{Re}\Delta = \mathrm{Re}(r_0/R)^3]$ and Δ. But Δ is a geometrical parameter, of much less physical relevance than the Reynolds number Re_0, and will be fixed to $\Delta=0.1$ in all the numerical results given

below (remember that the swirl parameter L has been fixed to $\sqrt{2}$).

Finally, the common part between the inviscid solution (16) and the boundary layer solution (18) is obtained by making $y\to\infty$ in (16) or, alternatively, $\gamma\to\infty$ in (18) resulting in[8]

$$\Psi_{\text{comm}}=\left(\frac{2rz}{\Delta}\right)^{1/2},\quad \Gamma_{\text{comm}}=L,\quad \Pi_{\text{comm}}=-\nabla_*^2\Psi_{\text{comm}}. \tag{23}$$

Substituting all these expressions into (13)–(15), one obtains the flow boundary conditions at $r=1$. Figure 2 shows the details of the matching for $\text{Re}_0=10$ and $\Delta=0.1$, and Fig. 3 depicts the boundary conditions for several values of Re_0 with $\Delta=0.1$.

The remaining boundary conditions for Eqs. (8)–(10) are the following: at the solid wall ($z=0$) the velocity field vanishes, implying that

$$\Psi(r,z=0)=0,\quad \Gamma(r,z=0)=0,\quad \Pi(r,z=0)=-\Delta^2\left(\frac{\partial^2\Psi}{\partial z^2}\right)_{z=0}; \tag{24}$$

at the axis ($r=0$) one has the symmetry conditions

$$\Psi(r=0,z)=\Gamma(r=0,z)=\Pi(r=0,z)=0, \tag{25}$$

and at $z=z_1\equiv z_f/z_0$ we assume that the second derivatives of the variables vanish,

$$\frac{\partial^2\Psi}{\partial z^2}=\frac{\partial^2\Gamma}{\partial z^2}=\frac{\partial^2\Pi}{\partial z^2}=0,\quad \text{at } z=z_1. \tag{26}$$

In the computations, we use different values of $z_1\geqslant 1$ in order to assure that the numerical solution does not depend on the specific value of z_1, where this last boundary condition is applied (remember that $z_0/r_0=\Delta^{-1}\gg 1$).

B. Numerical method

We are mostly interested in the steady-state solutions of the problem formulated above for different (increasing) values of the Reynolds number Re_0. For this reason, no initial condition has been specified. To obtain these steady solutions numerically, we use a continuation and bifurcation method very similar to that described in Sanchez *et al.*[19] Basically, the equations and boundary conditions (8)–(26), once discretized on $N\equiv(N_r+1)\times(N_z+1)$ spatial nodes, including the boundaries, are written in the vector compact form

$$\frac{\partial}{\partial t}\mathbf{B}\cdot\mathbf{x}=\mathbf{L}\cdot\mathbf{x}+\mathbf{N}(\mathbf{x},\mathbf{x})\equiv\mathbf{f}(\mathbf{x}\,.\,\text{Re}_0), \tag{27}$$

where $\mathbf{x}\equiv(\boldsymbol{\Psi},\boldsymbol{\Gamma},\boldsymbol{\Pi})^T$ is a vector of size $3N$ formed by the values of the variables Ψ, Γ, and Π on every spatial node, and $\mathbf{B}$, $\mathbf{L}$, and $\mathbf{N}$ are the discretized versions of the continuous linear and nonlinear operators in the equations and boundary conditions. The steady-state solutions are obtained by solving the corresponding time-independent equation $\mathbf{f}(\mathbf{x},\text{Re}_0)=0$, together with an additional condition, which allows us to follow the solution of this equation as the parameter Re_0 is varied. To be able to follow the solution in the presence of folds or bifurcations, a pseudo-arclength continuation method is used.[20] In terms of the continuation variable s along the curve of solutions, the equations to be solved are

$$\mathbf{f}(\mathbf{x},\text{Re}_0)\equiv\mathbf{L}\cdot\mathbf{x}+\mathbf{N}(\mathbf{x},\mathbf{x})=0 \tag{28}$$

and

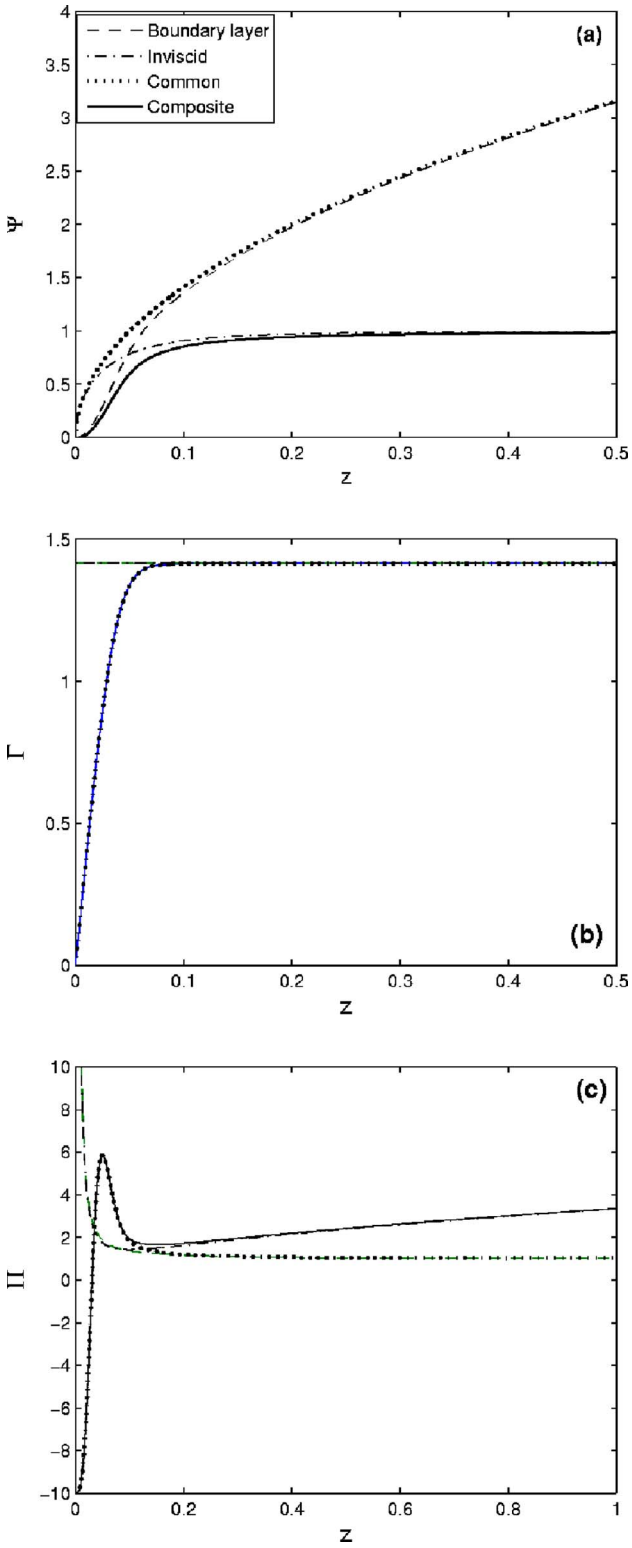

FIG. 2. (Color online) Matching details of the boundary conditions (13)–(15) for Ψ (a), Γ (b), and Π (c) at $r=1$, for $\text{Re}_0=10$, $\Delta=0.1$, and $L=\sqrt{2}$.

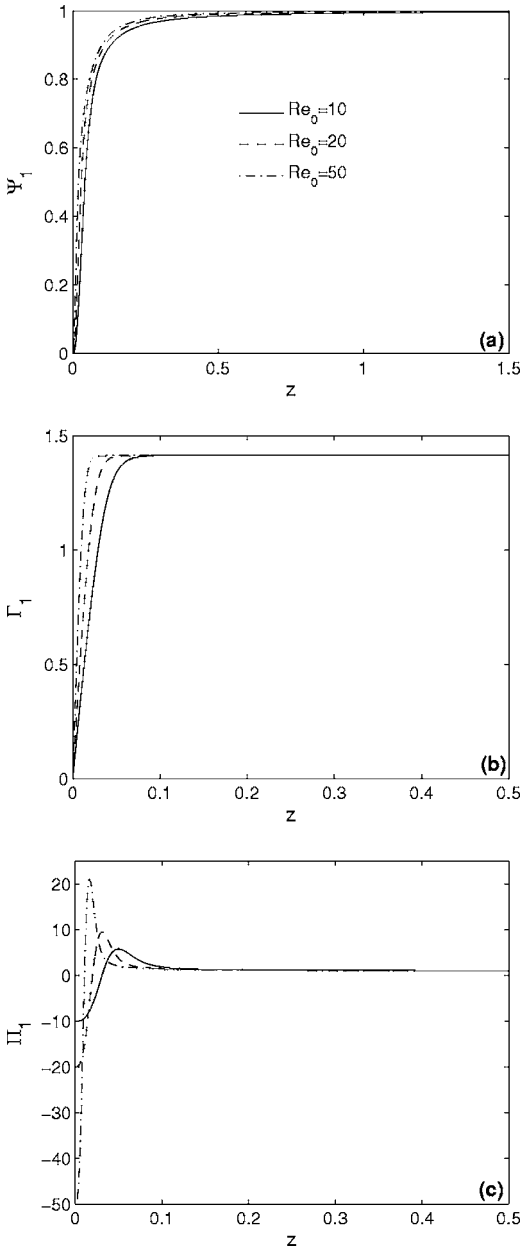

FIG. 3. Boundary conditions (13)–(15) for Ψ (a), Γ (b), and Π (c) at $r=1$, for $\Delta=0.1$, $L=\sqrt{2}$, and three values of Re_0, as indicated.

$$n(\mathbf{x},\mathrm{Re}_0) \equiv \frac{d\mathbf{x}}{ds}\cdot(\mathbf{x}-\mathbf{x}^0)+\frac{d\mathrm{Re}_0^0}{ds}(\mathrm{Re}_0-\mathrm{Re}_0^0)=0, \qquad (29)$$

where $(\mathbf{x}^0,\mathrm{Re}_0^0)$ is the predicted point along the curve of solutions in the space $(\mathbf{x},\mathrm{Re}_0)$, which is obtained by quadratic extrapolation from the three previous solutions along the curve for a given increment δs. Once this predicted point is obtained, the solution to (28) and (29) is found by a Newton-Raphson iteration method. To start this continuation method, one needs the steady solutions for three initial (low) values of Re_0. These are obtained by solving either the time-dependent equation (27) starting from the flow at rest, which is feasible for very low values of Re_0, or by solving the time-independent equation $\mathbf{f}(\mathbf{x},\mathrm{Re}_0)=\mathbf{0}$ starting from an initial approximate flow of the form

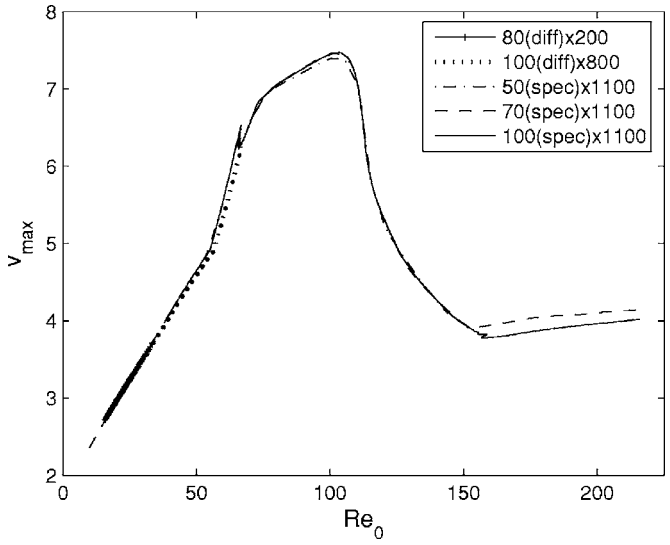

FIG. 4. Largest swirl in the whole domain, $v_{\max}$, as a function of Re_0 obtained with different meshes and numerical techniques. In the legend we specify N_r, the numerical technique in the radial direction (finite differences or spectral method), and N_z (in the z direction we always use finite differences on a nonuniform mesh).

$$\Psi(r,z)=\Psi_1(z)r^2, \quad \Gamma(r,z)=\Gamma_1(z)r^2, \quad \Pi(r,z)=\Pi_1(z)r^2, \qquad (30)$$

where Ψ_1, Γ_1, and Π_1 are the boundary conditions (13)–(15) at $r=1$. In the former case, the time-dependent equation is solved by a second-order predictor-corrector method with a time step δt, and in the second case we use a Newton-Raphson iteration method. In the computations given below, we have used a combination of all these methods to check the accuracy of the results, reserving the continuation method to pass the folds in Re_0.

For the spatial discretizations, we have used second-order finite differences on a nonuniform mesh,[21] concentrating the nodes near the plane and near the axis (i.e., for small z and r). The resulting sparse linear system of equations has been solved with the subroutines in the SPARSEKIT package (a basic tool kit for sparse matrix computations, version 2, http://www.users.cs.umn.edu/~saad/software/SPARSKIT/sparskit.html). Finally, to check the accuracy of the results we have used different mesh sizes (different values of N_r and N_z) and different nonuniform distribution of the nodes. In addition, a spectral collocation method in the radial direction, but maintaining the finite differences in the z direction, has been used. Typically, we have used values of N_r between 80 and 120, and values of N_z between 200 and 1100, depending on Re_0, so that the number of unknowns $3N$ ranges between just 48000 to almost 4×10^5.

Figure 4 compares results obtained from different grids and methods as Re_0 is varied. As the test value we use the maximum azimuthal velocity in the whole domain, $v_{\max}$, which is the most sensitive quantity to the numerical accuracy we have found. In addition, this maximum swirl will be used in the next section, among other flow magnitudes, to characterize the different transitions in the flow as Re_0 is varied. It is observed that, up to $\mathrm{Re}_0\simeq50$, finite differences,

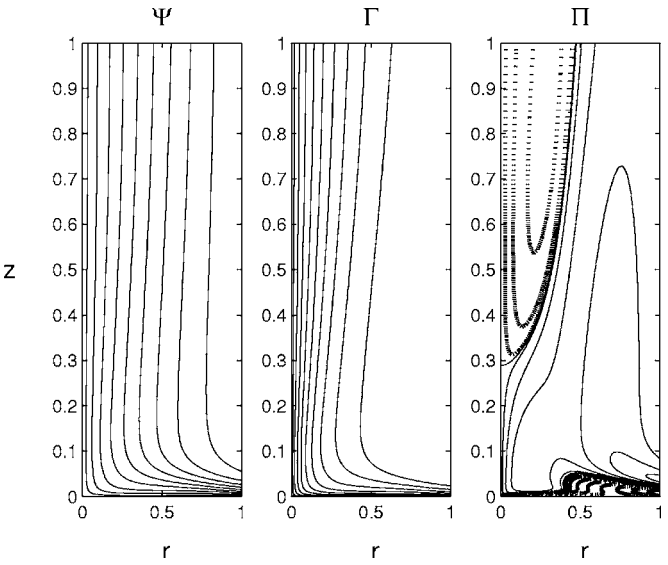

FIG. 5. Contour lines of Ψ, Γ, and Π (as indicated on the top of each subfigure) in the (r,z) plane for $\mathrm{Re}_0=15$, $L=\sqrt{2}$, and $\Delta=0.1$ (only the range $0\leqslant z\leqslant 1$ is shown). For each variable we plot with continuous lines 11 contour lines corresponding to $\Psi_{\max}(i/10)^3$, $\Gamma_{\max}(i/10)^3$, and $\Pi_{\max}(i/10)^3$, respectively, with $i=0,1,\ldots,10$. If there exists negative values of these variables, we also plot with dots 10 contour lines corresponding to $\Psi_{\min}(i/10)^3$, $\Gamma_{\min}(i/10)^3$, and $\Pi_{\min}(i/10)^3$, respectively, with $i=1,2,\ldots,10$ (in the present case, only the vorticity Π has negative values in the plotted domain).

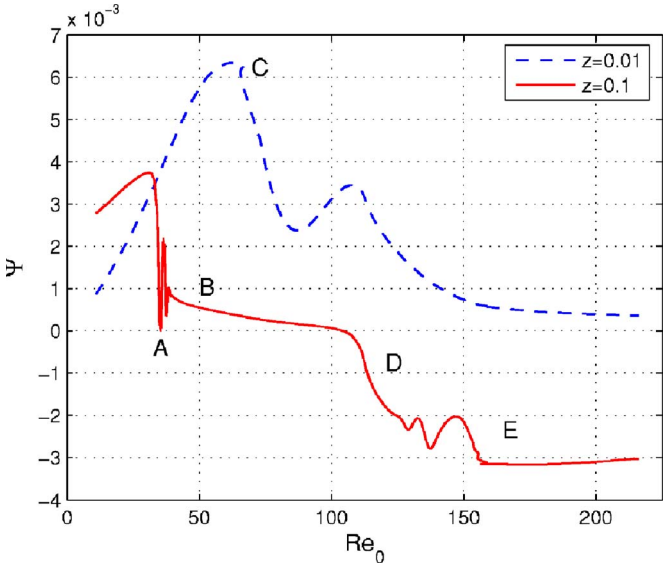

FIG. 6. (Color online) Ψ at $r=0.05$ and two values of z (as indicated) as a function of Re_0. The letters $A-E$ mark the different flow transitions.

and just $N_r\times N_z=80\times 200$ nodes, are enough to have a good accuracy. In fact, up to the first bifurcation ($\mathrm{Re}_0\simeq 66$, see the next section), finite differences provide good results with a reasonable number of nodes. However, after this bifurcation, the structure of the flow becomes more involved, especially near the origin, and the gradients near the solid plane are so large that the use of finite differences in the radial direction becomes prohibitive for our computer facility. For that reason, after that Reynolds number we use a spectral collocation technique in the radial direction, which is much more accurate for the same number of nodes, but at the cost of a more complex numerical code, and more computer memory for a given N_r, because the matrices become less sparse. However, one may use much smaller values of N_r for the same accuracy.[22] We use Chebyshev polynomials, with the spectral nodes $s_j=\cos(j\pi/N_r)$, $j=0,1,\ldots,N_r$, distributed in the radial direction according to the linear transformation $r_j=(1+s_j)/2$, which concentrates the nodes near the axis $r=0$ (and also near the boundary $r=1$). It is observed in Fig. 4 that this spectral method yields very accurate results with just $N_r=50$ (together with $N_z=1100$ finite-difference axial nodes very concentrated near the plane $z=0$) up to the second bifurcation ($\mathrm{Re}_0\sim 158$, see the next section). After that bifurcation, we have to increase the number of radial, spectral nodes to $N_r=100$. In most of the results reported below, we use $N_r=100$ spectral nodes in the radial direction and $N_z=1100$ finite-difference nodes in the axial direction.

III. RESULTS

We present here the different solutions of the problem for a given small value of $\Delta=0.1$ as the Reynolds number Re_0 is varied, which is the only parameter left in the problem once L has been fixed to $\sqrt{2}$. We also fix $z_1=5.7$, which is large enough for the solution to be independent of the boundary condition (26) for the highest values of Re_0 considered (for small Re_0 one may use much smaller values of z_1). Note that in all the results given below the vertical scale is actually $\Delta^{-1}=10$ times larger that the radial scale, so that the height of the computational domain is in fact 57 times larger than its radius. Also, the actual Reynolds number of the flow (12), based on r_0 and on the characteristic velocity V_0, is $\mathrm{Re}=\mathrm{Re}_0/\Delta=10\mathrm{Re}_0$.

To have a preliminary idea of the solution for a relatively low value of Re_0, Fig. 5 shows contour lines for Ψ, Γ, and Π in the (r,z) plane for $\mathrm{Re}_0=15$ (only the interval $0\leqslant z\leqslant 1$ is shown in the figure). For this Reynolds number, the flow is one-celled and smooth everywhere, entering at $r=1$ with the

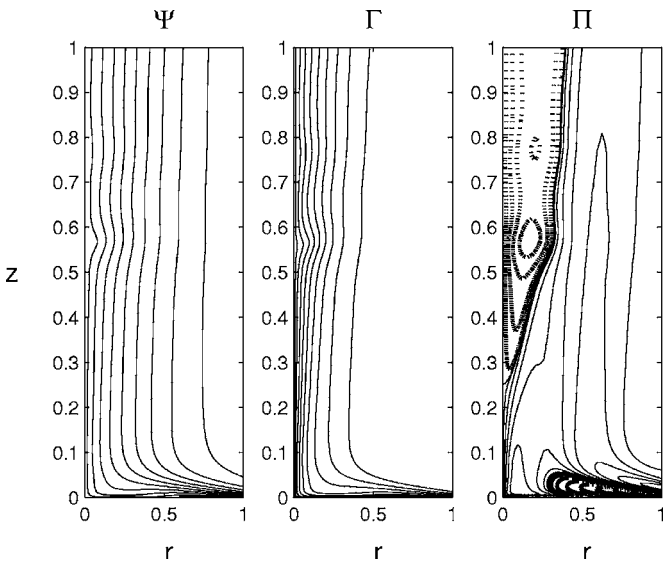

FIG. 7. As in Fig. 5, but for $\mathrm{Re}_0=34$.

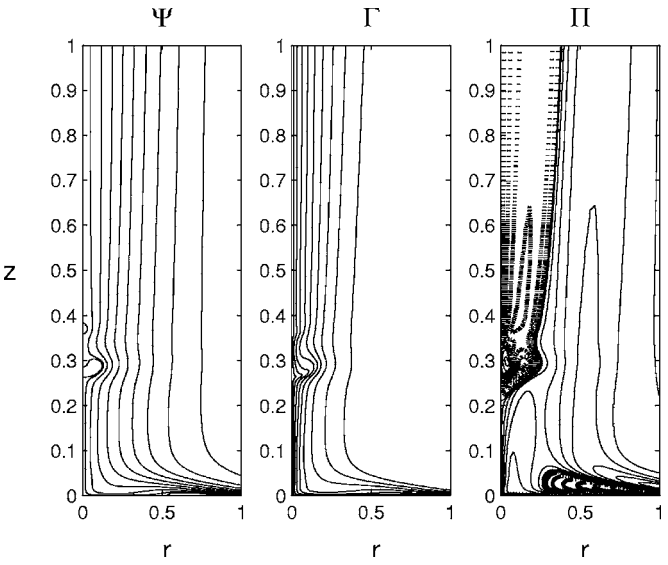

FIG. 8. As in Fig. 5, but for $\mathrm{Re}_0=40$.

flow rate mostly concentrated near the plane $z=0$, and turning upwards to exit the computational domain at its top. The flow is upwards all along the axis. The swirl intensifies near the axis, particularly near the plane, where the flow turns up.

As the Reynolds number increases, the flow becomes more and more involved, especially close to the plane $z=0$, undergoing several transitions in the form of vortex breakdown bubbles at the axis and other bifurcations. To visualize these transitions, we use Fig. 4 together with Fig. 6, which shows the value of Ψ as a function of Re_0 at two different points near the axis ($r=0.05$) at two different heights z very close to the surface. The maximum value of the Reynolds number we have reached is $\mathrm{Re}_0=216$ ($\mathrm{Re}=2160$). There are five main transitions, marked with the letters $A-E$ in Fig. 6, which are described next.

A. Vortex breakdown bubbles

At $\mathrm{Re}_0=\mathrm{Re}_0^A\simeq 34$ a breakdown bubble appears at the axis, just above $z=0.5$ (see Fig. 7). This is not a bifurcation of the solution in the parameter Re_0, but a smooth transition, quite similar to the first appearance of a breakdown bubble in Escudier's cell, as described, for instance, by Lopez.[23] The appearance of this breakdown bubble is preceded, as discussed by Brown and Lopez,[24] by a change in the sign of the local vorticity (see Fig. 7 for Π).

As the Reynolds number increases above Re_0^A, the breakdown bubble increases in size and moves downwards toward the solid plane. Eventually, at $\mathrm{Re}_0\simeq 38$, a second breakdown bubble appears just above the first one (see Fig. 8 for $\mathrm{Re}_0=40$). This transition is also smooth and very similar to that in Escudier's cell.[23] As Re_0 increases further, these two breakdown bubbles coalesce (see, e.g., Fig. 11 discussed below).

B. Swirl intensification near the surface

At $\mathrm{Re}_0=\mathrm{Re}_0^B\simeq 55$, the swirl intensifies abruptly near the surface $z=0$. This transition is not appreciated in Fig. 6, but it is in Fig. 4 as a change in the rate at which $v_{\max}$ increases with Re_0. In fact, the circulation does not change appreciably, but the height z at which the maximum swirl is located goes down abruptly at this Reynolds number [see Fig. 9(a)]. For $\mathrm{Re}_0>\mathrm{Re}_0^B$, the maximum swirl remains very close to the surface (below $z=0.01$). The location of the maximum swirl also approaches abruptly to the axis at $\mathrm{Re}_0=\mathrm{Re}_0^B$ [see Fig. 9(b)]. This intensification of the swirl near $z=0$, which is a consequence of the breakdown bubbles traveling toward the floor, is relevant because it makes possible the bifurcation described next.

C. First bifurcation, third breakdown bubble

Point C in Fig. 6 corresponds to a bifurcation in the solution, where in a small interval of Reynolds numbers, $\mathrm{Re}_0^{C1}\simeq 65.58<\mathrm{Re}_0<\mathrm{Re}_0^{C2}\simeq 66.87$ (see zoom in Fig. 10), three different solutions coexist for the same Re_0. A close view near the origin of the different solutions for $\mathrm{Re}_0\approx 66$, marked in Fig. 10 with 1, 2, and 3, is depicted in Figs. 11–13. The solutions 1 and 2 are quite similar (Figs. 11 and 12), with a unique large breakdown bubble at the axis between

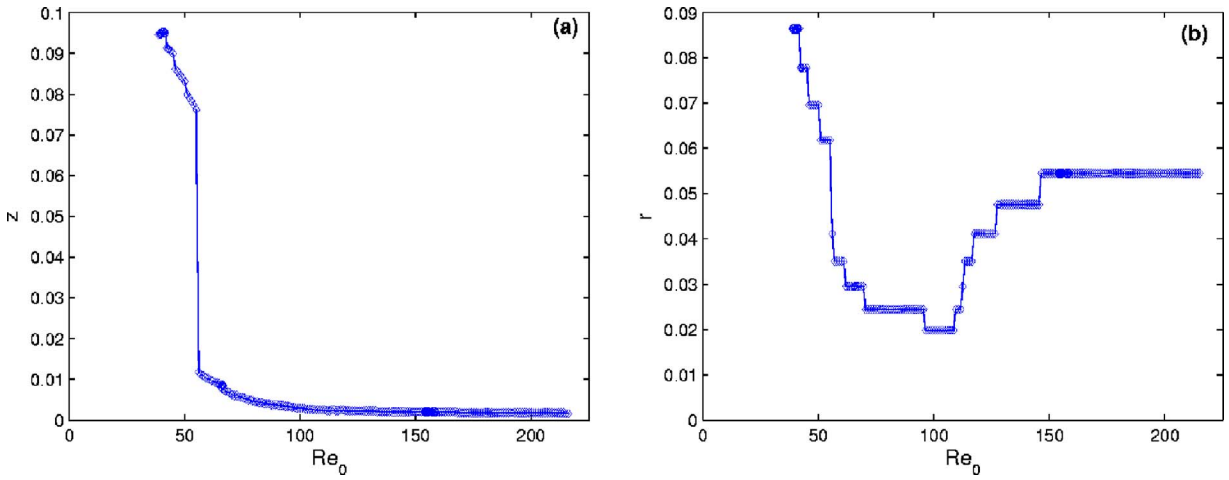

FIG. 9. (Color online) Height z (a) and radius r (b) at which the swirl is a maximum in the whole flow domain as functions of Re_0. These are the locations of $v_{\max}$ in Fig. 4.

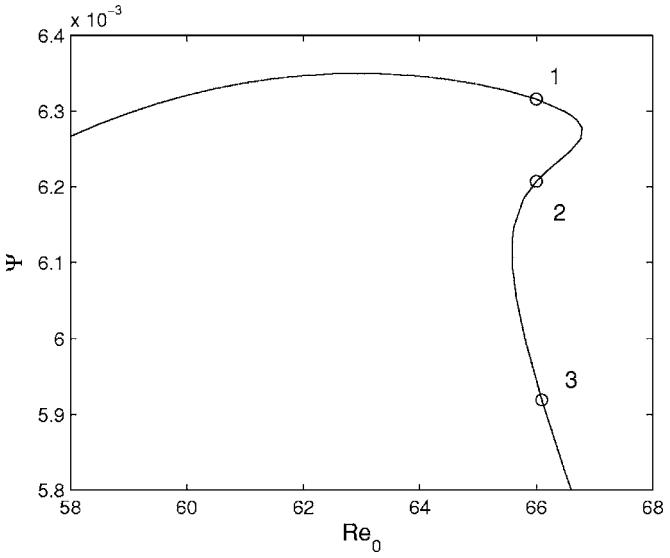

FIG. 10. Detail of the curve for $z=0.01$ in Fig. 6 near the bifurcation C.

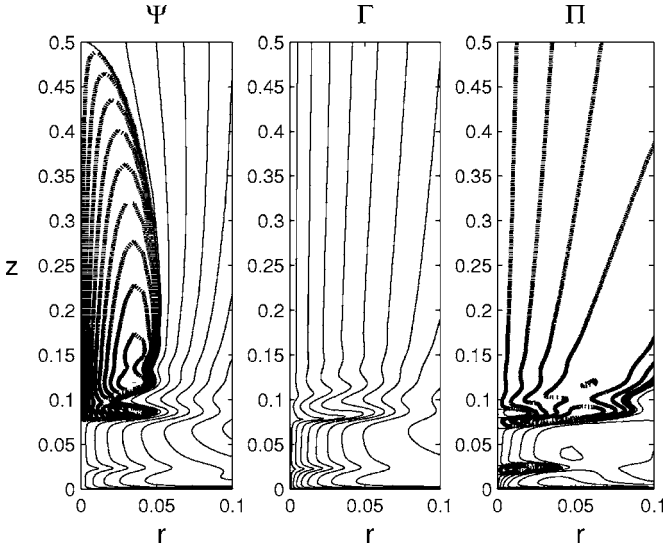

FIG. 12. Contour lines corresponding to the solution in point 2 of Fig. 10. $\mathrm{Re}_0=66.0021$.

$z\simeq 0.075$ and $z\simeq 0.5$, which comes from the coalescence of the two previous breakdown bubbles. However, solution 3 (Fig. 13) is qualitatively different, with a new vortex breakdown bubble very close to the plane, small but very intense, since the swirl is very concentrated at the axis near the plane after transition B. The formation of this new vortex breakdown bubble is thus qualitatively different from the previous smooth transition A, being similar to the vortex breakdown bifurcation in pipes described by Beran and Culik[25] and by Lopez.[26] As Re_0 increases above $\mathrm{Re}_0^{C2}\simeq 66.87$, the solution changes abruptly from type 1 to type 3, with a new vortex breakdown bubble very close to the plane. Conversely, if Re_0 now decreases below $\mathrm{Re}_0^{C1}\simeq 65.58$, the solution changes abruptly from type 3 to type 1, during which the lower breakdown bubble disappears, thereby closing the hysteresis cycle. This type of transition was theoretically studied for inviscid swirling flows in pipes by Wang and Rusak.[27] Solutions of type 2 are unstable and would never occur in practice. From a numerical point of view, the Jacobian associated to Eq. (27) becomes singular at Re_0^{C2} (Re_0^{C1}), requiring a continuation method to pass through it in the solution curve for increasing (decreasing) Reynolds numbers.[19,25,26]

D. Transition to Type II, or two-cell, solution

As Re_0 increases further, the breakdown bubbles in Fig. 13 coalesce, and the recirculating zone increases in size upwards along the axis until, eventually, it reaches suddenly the upper (exit) surface when $\mathrm{Re}_0=\mathrm{Re}_0^D\simeq 113$. For larger Re_0, the flow comes down at the axis from the upper surface $z=z_1$. The process is shown in Fig. 14, where the streamlines for three increasing values of Re_0 are plotted (note that the full scale in z is now plotted). The abruptness of the transition can be observed in Fig. 15, where we plot the height z of

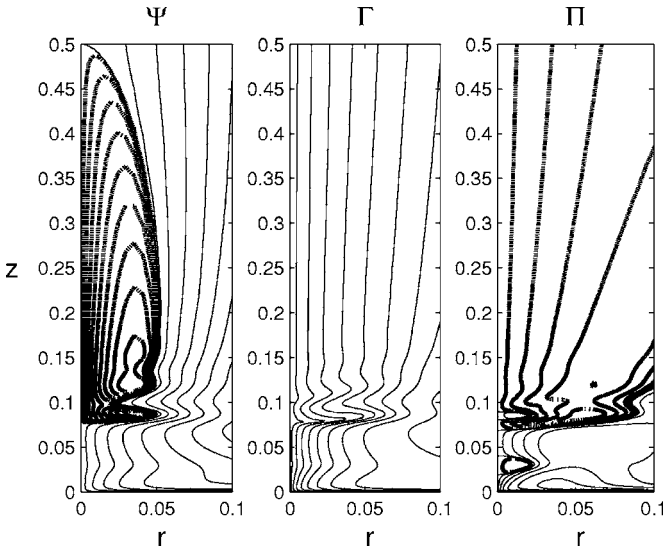

FIG. 11. Contour lines corresponding to the solution in point 1 of Fig. 10. $\mathrm{Re}_0=66.0$. (Contours as in Fig. 5.)

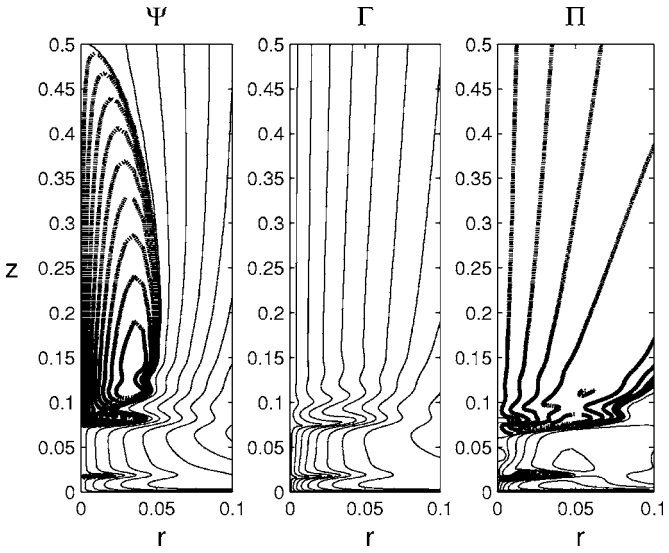

FIG. 13. Contour lines corresponding to the solution in point 3 of Fig. 10. $\mathrm{Re}_0=66.0971$.

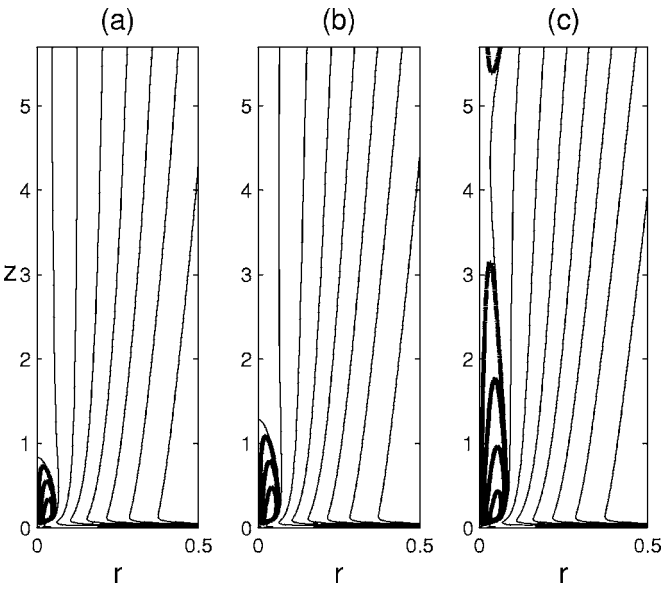

FIG. 14. Contour lines of Ψ for $\mathrm{Re}_0=105$ (a), 110 (b), and 113 (c). Note that the whole domain in z is now plotted, while only the interval $0\leqslant r\leqslant 0.5$ is shown.

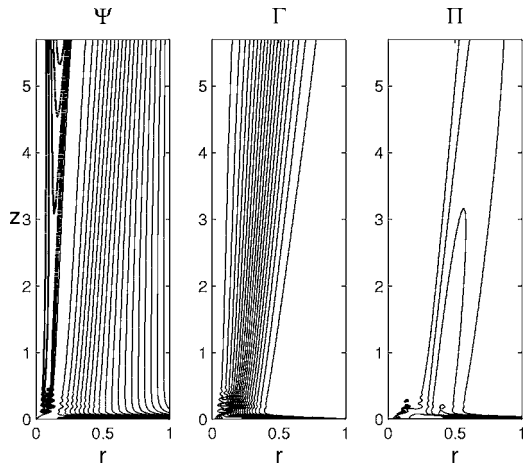

FIG. 16. Contour lines of Ψ, Γ, and Π in the (r,z) plane for $\mathrm{Re}_0=125$, $L=\sqrt{2}$, and $\Delta=0.1$. Of each variable we plot 21 equidistant contour lines between zero and their maximum values, and 20 equidistant contour lines between their (negative) minimum values (if they exist) and zero.

the upper stagnation point of the breakdown bubbles as a function of Re_0, showing a vertical asymptote at $\mathrm{Re}_0\simeq 113$. Therefore, the computed value of this critical Reynolds Re_0^D is almost independent of the computational height z_1, provided it is sufficiently large.

For $\mathrm{Re}_0>\mathrm{Re}_0^D$, most of the axis, from the top $z=z_1$ to almost the plane $z=0$, has negative axial velocity at the axis; i.e., we have a two-celled solution in most of the flow, which in the notation of the self-similar viscous solutions near the axis is termed as a solution of Type II.[11,12] Actually, the flow becomes almost columnar near the axis once this critical value has been surpassed (see Fig. 16 for $\mathrm{Re}_0=125$), with the central downdraft region in almost solid body rotation. The swirl in the annular updraft region becomes intensified as Re_0 increases. This behavior can be observed in Fig. 17, where we plot the radial profiles of the azimuthal and axial velocity components at $z=2$ for increasing values of Re_0. The intensification of the swirl in a transition from a one-cell to a two-cell flow structure is a well known phenomenon in the tornado literature.[28,29] However, the maximum swirl in the whole domain, which is located near the solid plane (see Fig. 9), decreases after this transition (Fig. 4) because the central slow downflow now approaches the ground. Another consequence of this transition is the formation of axial, axisymmetric standing waves in the lower part of the annular updraft region, which can already be observed in Fig. 16 for $\mathrm{Re}_0=125$. As we shall see below, these spatial undulations are intensified as Re_0 increases. They are typical of the viscous interaction of a solid-body rotating flow, like that inside the annular updraft, with the ground, or Bödewadt-type flows.[1,16,18]

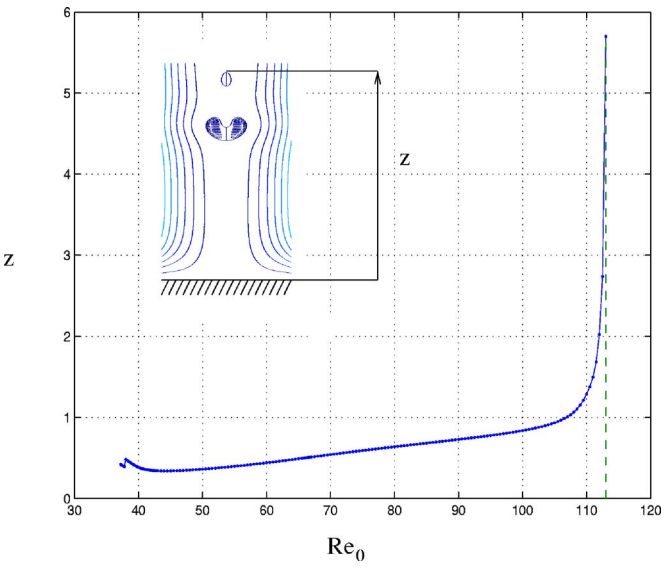

FIG. 15. (Color online) Evolution with Re_0 of the height z of the uppermost stagnation point at the axis of the breakdown bubble.

E. Second bifurcation, self-similar solutions

As the Reynolds number increases further, the flow near the axis and far from the ground *must* approach Long's self-similar solutions. In fact, according to the results of the above section III D, they must approach a two-celled, or Type II, self-similar solution, with negative axial velocity at the axis. We find that this is the case but, before that asymptote is reasonably accurate, there exists a second bifurcation in the flow similar to that in *C*: in a small interval of Reynolds numbers, $\mathrm{Re}_0^{E3}\simeq 156.65<\mathrm{Re}_0<\mathrm{Re}_0^{E1}\simeq 158.5$ (see zoom in Fig. 18), three different solutions coexist for the same Re_0. That marked in Fig. 18 with 3 for $\mathrm{Re}_0=157.8$ is depicted in Fig. 19. The other two solutions, marked in Fig. 18 with 1 and 2, are quantitatively very similar, because the intensity of the bifurcation is in fact very small, and are not shown. But there exists a qualitative difference in the evolution of the solutions after this bifurcation that affects all the subsequent solutions for $\mathrm{Re}_0>\mathrm{Re}_0^{E1}$.

This bifurcation corresponds to the Reynolds numbers at

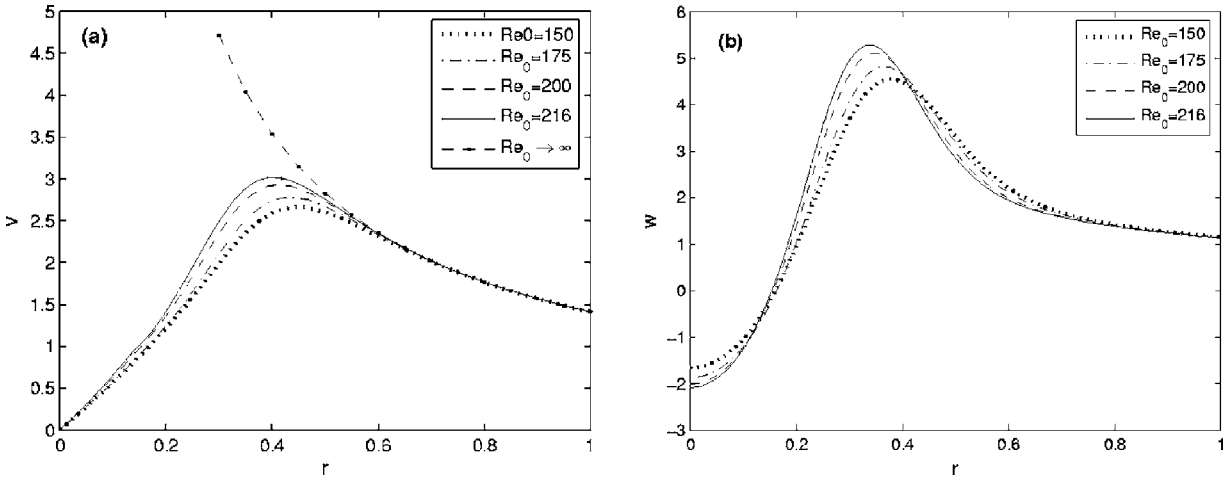

FIG. 17. (a) Radial profiles of the azimuthal velocity at $z=2$ for different values of Re_0. Also plotted is the inviscid behavior L/r (boundary condition at $r=1$). (b) Radial profiles of the axial velocity for the same values of Re_0.

which the downdraft region reaches the ground, with the lower stagnation point below the region of recirculating flow jumping from the axis to the solid plane (Fig. 19). We observe in Figs. 4, 6, and 9 that once this bifurcation is passed for $\mathrm{Re}_0 > \mathrm{Re}_0^{E1} \simeq 158$, the global behavior of the flow changes, in the sense that its subsequent evolution as Re_0 increases becomes smooth, particularly near the ground. Thus, for instance, the solution for $\mathrm{Re}_0=175$ shown in Fig. 20 is qualitatively very similar to that shown in Fig. 19. In fact, as we shall see next, suddenly starting from Re_0^{E1}, the flow far from the ground compares very well with Long's similarity solutions. That is to say, this transition seems to mark the onset for the self-similar behavior of the solutions for large Reynolds numbers at large z.

To make this comparison, we first look for a representation of the numerical solutions, which allow us to see how far we are from a similarity solution at all. To that end, we define the variables

$$\rho = \frac{r}{r_{\max}(z)}, \quad V = \frac{v}{v_{\max}(z)}, \quad W = \frac{w}{v_{\max}(z)}, \tag{31}$$

where $v_{\max}(z)$ is the maximum value of the azimuthal velocity component for a given height z and $r_{\max}(z)$ is its radial location. Figure 21 shows V and W as functions of ρ for several heights z between 3 and z_1, and for four values of Re_0 (the same values considered in Fig. 17 for $z=2$). We observe the collapse of the solutions, especially for the last three values of Re_0, which are larger that Re_0^{E1}, thus showing that the solution far from the ground tends to a similarity solution, the more so the higher the Reynolds number. These variables ρ, V, and W correspond (are proportional) to Long's similarity variables if[9,11]

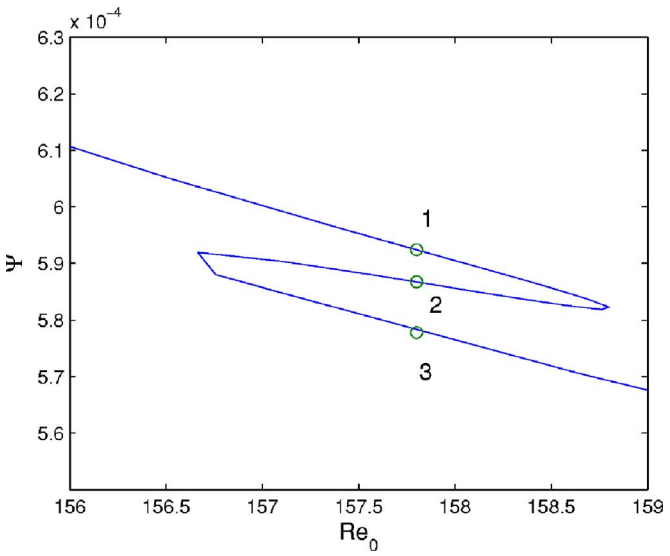

FIG. 18. (Color online) Detail of the curve for $z=0.1$ in Fig. 6 near the bifurcation E.

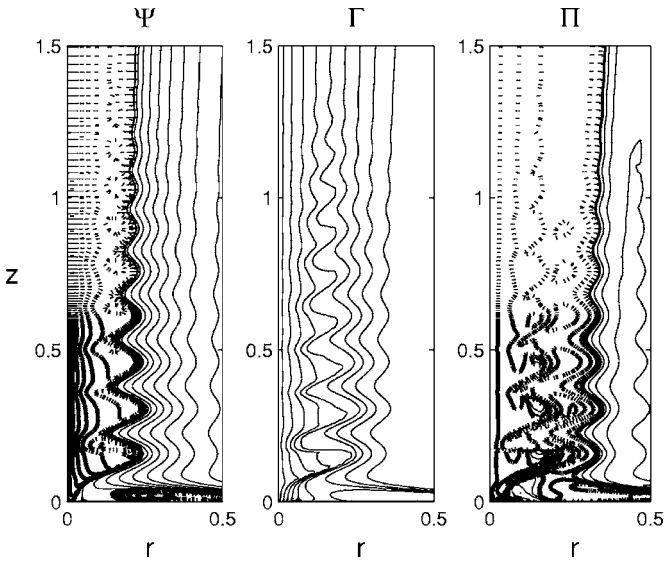

FIG. 19. Contour lines near the origin corresponding to the solution in point 3 of Fig. 18. $\mathrm{Re}_0=157.8$. (Contours as in Fig. 5.)

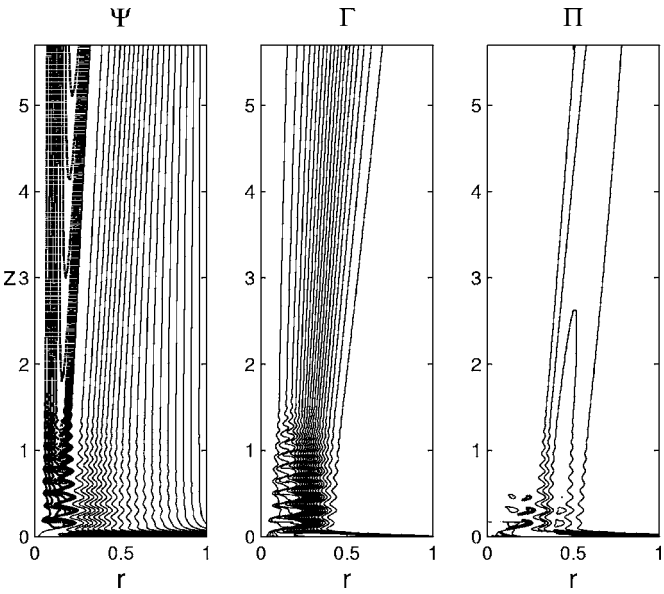

FIG. 20. As in Fig. 16, but for $\mathrm{Re}_0=175$.

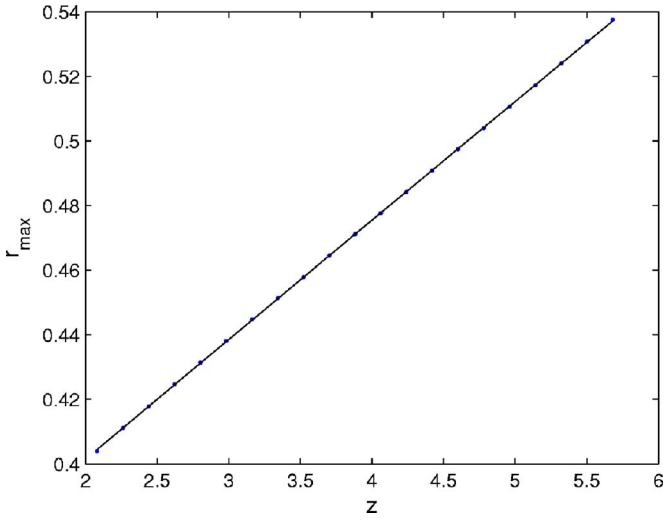

FIG. 22. Computed values of $r_{\max}(z)$ for $\mathrm{Re}_0=216$ (dots) which are adjusted with $r_{\max}=0.0441[(z+8.245)/\mathrm{Re}_0]^{0.95}$.

$$r_{\max}(z;\mathrm{Re}_0)\sim\left(\frac{z}{\mathrm{Re}_0}\right)^{n_1},\quad v_{\max}(z;\mathrm{Re}_0)\sim\left(\frac{\mathrm{Re}_0}{z}\right)^{n_2}\qquad(32)$$

for large z and $\mathrm{Re}=\mathrm{Re}_0/\Delta$, with $n_1=n_2=1$ for Long's vortex ($m=1$ in the notation of Ref. 11). Figure 22 shows that, for $\mathrm{Re}_0=216$, the above behavior with $r_{\max}$ a power function of z is very accurate, but with n_1 slightly smaller than unity. In fact, as is shown in Fig. 23, where the powers n_1 and n_2 obtained numerically are plotted as functions of Re_0, both n_1

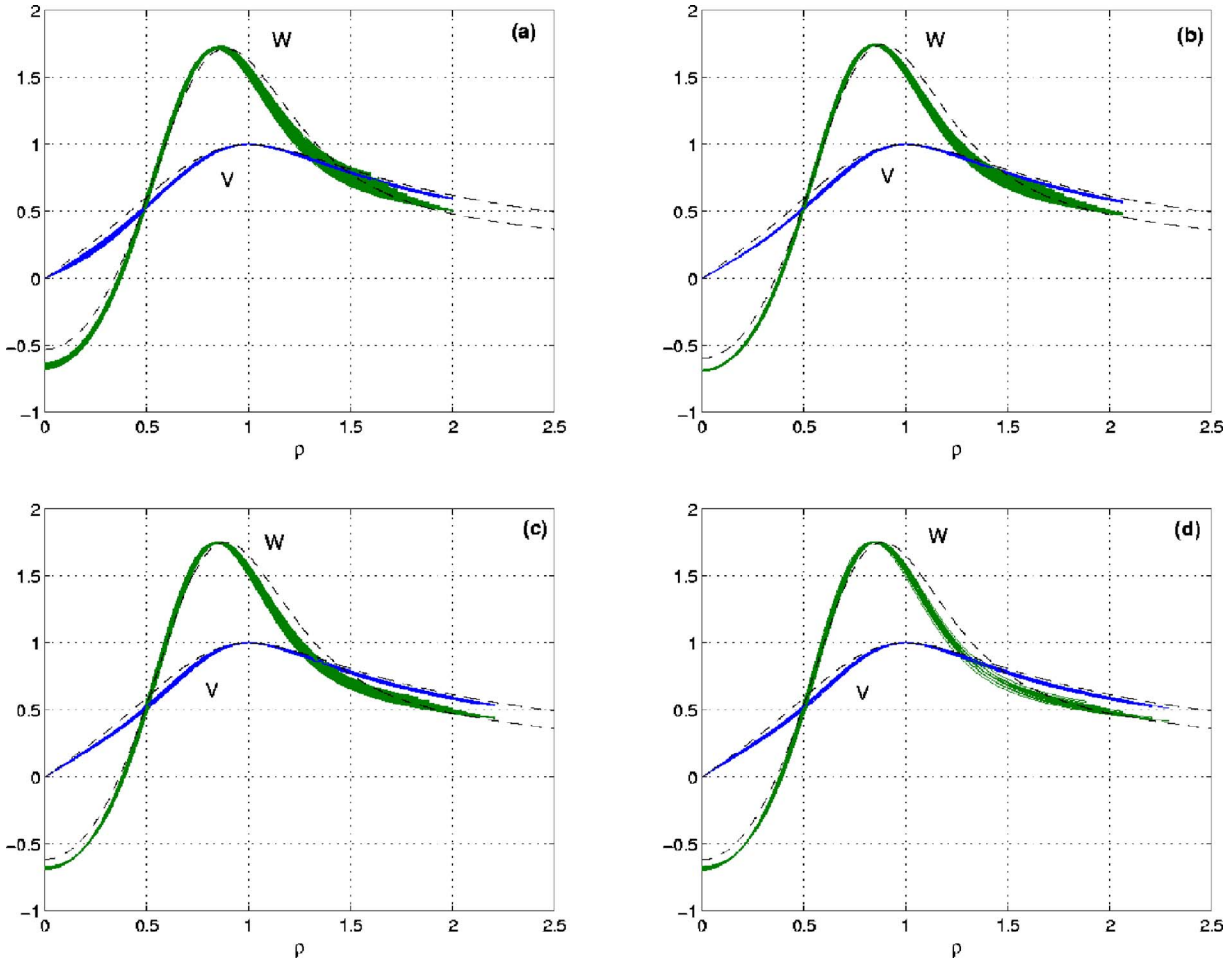

FIG. 21. (Color online) $V(\rho)$ and $W(\rho)$ at $z=3,3.18,3.32,\ldots,5.7$ for $\mathrm{Re}_0=150$ (a), $\mathrm{Re}_0=175$ (b), $\mathrm{Re}_0=200$ (c), and $\mathrm{Re}_0=216$ (d). With dashed lines we show the corresponding Long's self-similar solution.

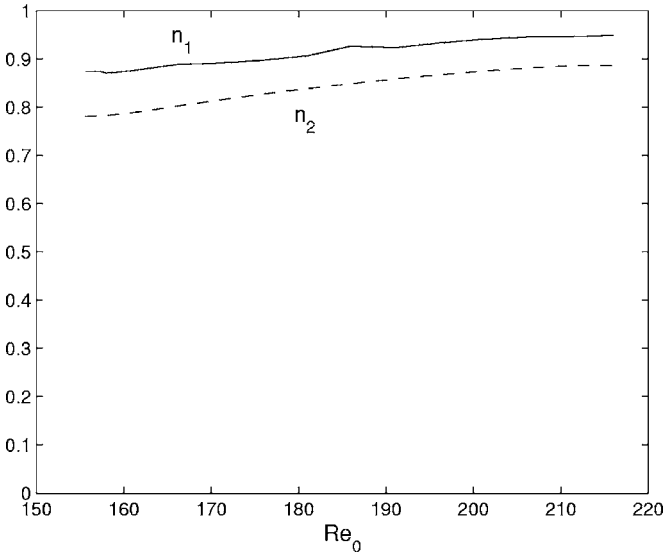

FIG. 23. Computed values n_1 (continuous line) and n_2 (dashed line) as a function of Re_0.

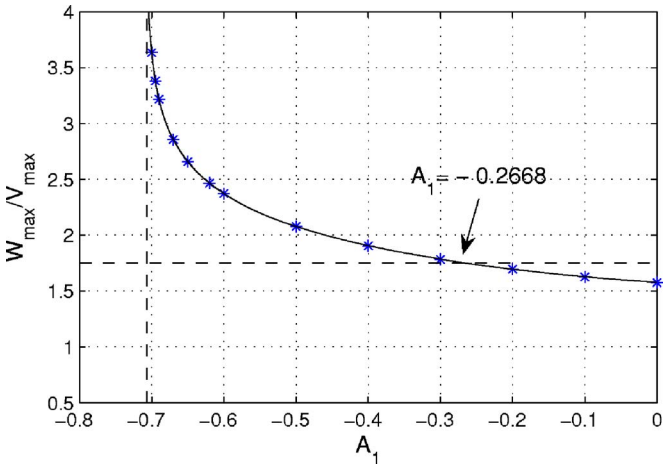

FIG. 25. (Color online) $W_{\max}/V_{\max}$ as a function of $A_1(\leqslant 0)$ for Long's self-similar solution (from Fig. 24). We have marked with a horizontal dashed line the case corresponding to $\mathrm{Re}_0=216$, and with a vertical dashed line the minimum value of A_1, $-1/\sqrt{2}$.

and n_2 are very close to unity for $\mathrm{Re}_0 > \mathrm{Re}_0^{E1} \simeq 158$, and tend (slowly) to unity as Re_0 increases.

To make a quantitative comparison of the numerical velocity profiles with the self-similar solutions, we have to adjust the proportionality constants missing in (32) to those appearing in Long's similarity variables. In addition, Long's similarity solution is not unique, but there exists a multiplicity of solutions, each of them characterized by a different value of the nondimensional axial velocity at the axis, which in Ref. 11 is termed as $2A_1$. One of the best ways to adjust all this is by computing $W_{\max}/V_{\max}$ ($=W_{\max}$ since $V_{\max}\equiv 1$ by definition) for each Re_0, and selecting the value of A_1 in Long's similarity solution for the same value of $W_{\max}/V_{\max}$. Figure 24 shows Long's similarity solution for different values of A_1,[11] and Fig. 25 depicts the ratio $W_{\max}/V_{\max}$ computed from that figure as a function of A_1 in its negative range $-1/\sqrt{2} < A_1 \leqslant 0$. On the other hand, Fig. 26 shows $W_{\max}/V_{\max}$ obtained from the numerical simulations as function of Re_0. (Note in this figure how the behavior changes at the critical Reynolds number $\mathrm{Re}_0=\mathrm{Re}_0^{E1}\simeq 158$, as commented on above.) Thus, comparing Figs. 25 and 26 we can select the corresponding values of A_1 and, therefore, the corresponding member of the family of Long's self-similar solution for each value of Re_0 (see Fig. 27). Making use of these values $A_1(\mathrm{Re}_0)$, we have included with dashed lines in Fig. 21 the corresponding Long's self-similar solution for each value of Re_0. It is observed that the agreement is quite good, particularly for the three last cases; i.e., for $\mathrm{Re}_0 > \mathrm{Re}_0^{E1}$.

In Fig. 28, we have plotted the nondimensional flow force M in Long's vortex corresponding to each A_1 (i.e., Fig. 2 in Ref. 30, which is reproduced here for convenience), showing the existence of two different solutions, termed Type I and Type II,[12] for each value of M. Clearly, the solutions found here numerically are of Type II with $A_1<0$. Making use of this figure, together with Fig. 27, we have plotted in Fig. 29 the corresponding Long's nondimensional

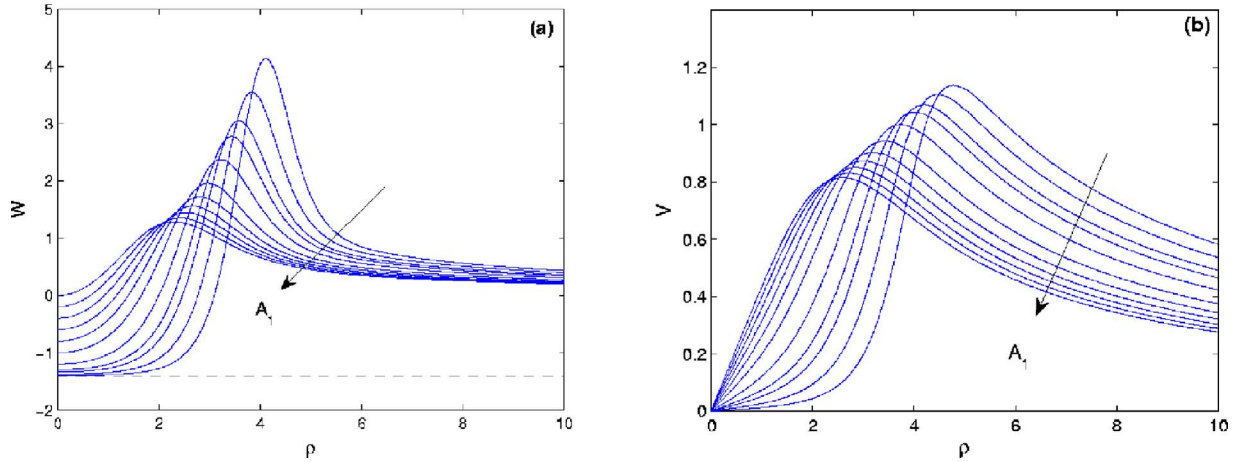

FIG. 24. (Color online) Long's self-similar velocity profiles for $W(\rho)$ (a) and $V(\rho)$ (b) for different (nonpositive) values of the axial velocity at the axis.[11] In particular, the nondimensional axial velocity at the axis is $2A_1$, and we plot the profiles for $A_1=0$, -0.1, -0.2, -0.3, -0.4, -0.5, -0.6, -0.65, -0.67, -0.69, and -0.7. The minimum possible value, corresponding to $A_1=-1/\sqrt{2}\simeq -0.7071$, is plotted with a dashed line in (a).

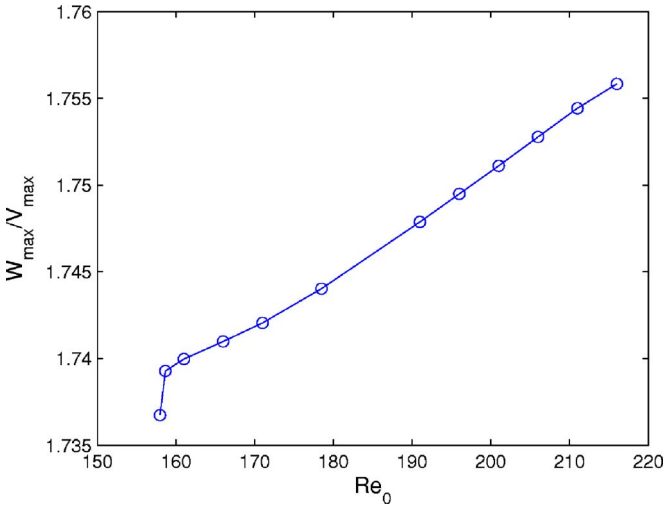

FIG. 26. (Color online) W_{max}/V_{max} as a function of Re_0 from the numerical computations.

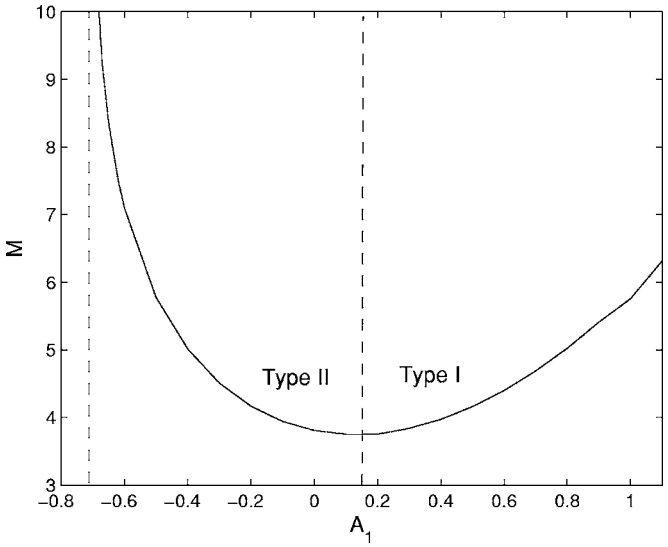

FIG. 28. Flow force M in Long's vortex as a function of A_1 showing the two different types of self-similar solutions for each M (from Ref. 30).

flow force M of the numerical solutions as a function of Re_0. It is observed that, for Re_0 larger than approximately Re_0^{E1}, the flow force evolves linearly with Re_0. This seems to indicate that as $Re_0 \to \infty$ the solution far from the ground tends to Long's self-similar solution with the lowest possible axial velocity at the axis, i.e., with $A_1 \to -1/\sqrt{2}$. However, we have not been able with our computer facilities to reach values of Re_0 larger than approximately 216 ($Re = Re_0/\Delta = 2160$).

IV. SUMMARY AND CONCLUSIONS

We have considered here the interaction of a quite general type of axisymmetric free vortex with a solid plane perpendicular to its axis by solving numerically the full incompressible Navier-Stokes equations. For high Reynolds numbers, and far from the plane, this family of vortices corresponds to the inviscid outer behavior of Long's vortex, commonly used as a model of tornado-like vortices.[12,31] As the radial inflow boundary condition far from the axis, we have used this inviscid solution matched asymptotically with the corresponding viscous boundary layer on the plane.[8] The problem is formulated in such a way that it depends on a unique Reynolds number Re_0. For moderately low Reynolds numbers, we find smooth, one-celled solutions. As the Reynolds number increases, several vortex breakdown bubbles with flow recirculation are formed at the axis relatively close to the plane. The last breakdown bubble formed as the Reynolds number is increased, which is the closest to the plane, is associated with a bifurcation of the equation with multiplicity of solutions, similar to that found by Beran and Culik[25] and by Lopez[26] for vortex breakdown in a pipe. Eventually, all the breakdown bubbles coalesce and, for a Reynolds number above a critical value, the flow acquires a two-celled structure, with a downdraft axial flow at the axis and an annular updraft region around it where the swirl is intensified. This two-celled structure is in agreement with the observed flow in mature tornadoes. After a second bifurca-

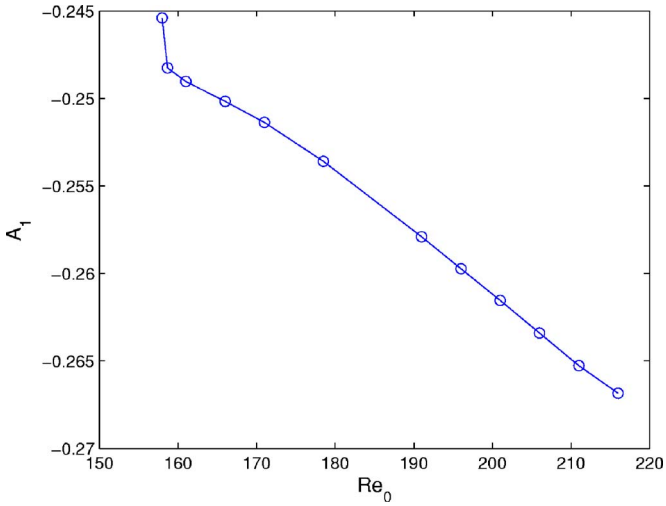

FIG. 27. (Color online) $A_1(Re_0)$ computed from Figs. 25 and 26.

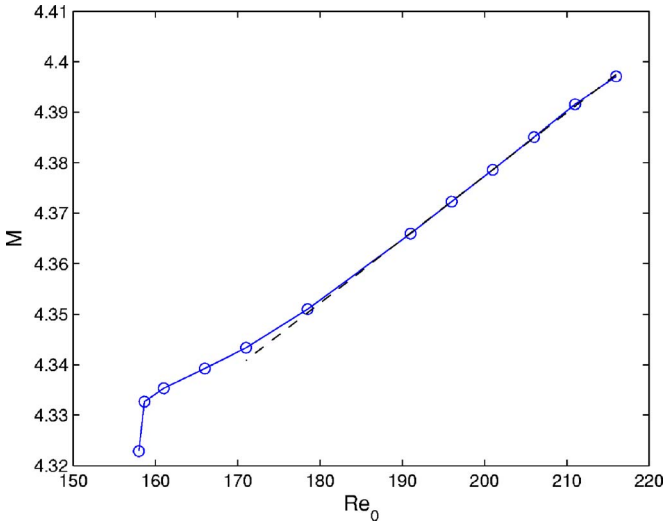

FIG. 29. (Color online) Flow force M as a function of Re_0 computed from Figs. 27 and 28. The dashed line corresponds to $M \simeq 0.0013 Re_0 + 4.1258$.

tion, the axial downdraft reaches the ground and we find that far from the solid plane the two-cell flow structure compares quite well with Long's self-similar solutions of Type II,[9,11,12] with negative axial velocity at the axis ($A_1<0$) and a flow force (M), which depends almost linearly with the Reynolds number Re_0. As Re_0 increases, A_1 decreases and M increases, in such a way that for $\mathrm{Re}_0\to\infty$ the flow above the ground tends to a two-celled structure with an almost quiescent potential vortex core surrounded by an annular updraft of infinite intensity, corresponding to $M\to\infty$ and $A_1\to-1/\sqrt{2}$ in Long's self-similar solution.

ACKNOWLEDGMENTS

This work has been supported by the Ministerio de Educación y Ciencia of Spain (Grant No. FIS2004-00538). The numerical computations have been made in the computer facility "Taylor" at the ETSII of the University of Málaga.

[1] U. T. Bödewadt, "Die drehströmung über festem grunde," ZAMM **20**, 241 (1940).
[2] H. Schlichting, *Boundary Layer Theory*, 6th ed. (McGraw-Hill, New York, 1968).
[3] G. I. Taylor, "The boundary layer in the converging nozzle of a swirling atomizer," Q. J. Mech. Appl. Math. **3**, 129 (1950).
[4] W. S. King and W. S. Lewellen, "Boundary-layer similarity solutions for rotating flows with and without magnetic interaction," Phys. Fluids **7**, 1674 (1964).
[5] O. R. Burggraf, K. Stewartson, and R. J. Belcher, "Boundary layer induced by a potential vortex," Phys. Fluids **14**, 1821 (1971).
[6] R. J. Belcher, O. R. Burggraf, and K. Stewartson, "On generalized-vortex boundary layers," J. Fluid Mech. **52**, 753 (1972).
[7] T. S. Prahlad and M. R. Head, "Numerical solutions for the boundary layers beneath a potential vortex," Comput. Fluids **4**, 157 (1976).
[8] R. Fernandez-Feria and J. C. Arrese, "Boundary layer induced by a conical vortex," Q. J. Mech. Appl. Math. **53**, 609 (2000).
[9] R. R. Long, "A vortex in an infinite fluid," J. Fluid Mech. **11**, 611 (1961).
[10] R. Fernandez-Feria, J. Fernandez de la Mora, M. Perez-Saborid, and A. Barrero, "Conically similar swirling flows at high Reynolds numbers," Q. J. Mech. Appl. Math. **52**, 1 (1999).
[11] R. Fernandez-Feria, J. Fernandez de la Mora, and A. Barrero, "Solution breakdown in a family of self-similar nearly inviscid axisymmetric vortices," J. Fluid Mech. **305**, 77 (1995).
[12] O. R. Burggraf and M. R. Foster, "Continuation or breakdown in tornado-like vortices," J. Fluid Mech. **80**, 685 (1977).
[13] M. Perez-Saborid, M. A. Herrada, A. Gomez-Barea, and A. Barrero, "Downstream evolution of unconfined vortices: Mechanical and thermal aspects," J. Fluid Mech. **471**, 51 (2002).
[14] W. R. C. Phillips, "On vortex boundary layers," Proc. R. Soc. London, Ser. A **400**, 253 (1985).
[15] W. R. C. Phillips and B. C. Khoo, "The boundary layer beneath a Rankine-like vortex," Proc. R. Soc. London, Ser. A **411**, 177 (1987).
[16] A. Hirsa, J. M. Lopez, and S. Kim, "Evolution of an initially columnar vortex terminating normal to a no-slip wall," Exp. Fluids **29**, 309 (2000).
[17] R. D. Sullivan, "A two-cell vortex solution of the Navier-Stokes equations," J. Aero-Space Sci. **26**, 767 (1959).
[18] J. M. Lopez and P. D. Weidman, "Stability of stationary endwall boundary layers during spin-down," J. Fluid Mech. **326**, 373 (1996).
[19] J. Sanchez, F. Marques, and J. M. Lopez, "A continuation and bifurcation technique for Navier-Stokes flows," J. Comput. Phys. **180**, 78 (2002).
[20] H. B. Keller, "Numerical solution of bifurcation and nonlinear eigenvalue problems," in *Applications of Bifurcation Theory*, edited by P. Rabinowich (Academic, San Diego, 1977), pp. 359–384.
[21] E. Sanmiguel-Rojas, J. Ortega-Casanova, C. del Pino, and R. Fernandez-Feria, "A Cartesian grid finite-difference method for 2D incompressible viscous flows in irregular geometries," J. Comput. Phys. **204**, 302 (2005).
[22] C. Canuto, M. Y. Hussaini, A. Quarteroni, and T. A. Zang, *Spectral Methods in Fluid Dynamics* (Springer-Verlag, New York, 1988).
[23] J. M. Lopez, "Axisymmetric vortex breakdown. Part 1: Confined swirling flow," J. Fluid Mech. **221**, 533 (1990).
[24] G. L. Brown and J. M. Lopez, "Axisymmetric vortex breakdown. Part 1: Physical mechanisms," J. Fluid Mech. **221**, 553 (1990).
[25] P. Beran and F. Culik, "The role of nonuniqueness in the development of vortex breakdown in tubes," J. Fluid Mech. **242**, 491 (1992).
[26] J. M. Lopez, "On the bifurcation structure of axisymmetric vortex breakdown in a constricted pipe," Phys. Fluids **6**, 3683 (1994).
[27] S. Wang and Z. Rusak, "The dynamics of a swirling flow in a pipe and transition to axisymmetric vortex breakdown," J. Fluid Mech. **340**, 177 (1997).
[28] P. Dergarabedian and F. Fendell, "One- and two-cell structure in tornadoes," in *Proceedings of the Symposium on Tornadoes: Assessment of Knowledge and Implications for Man*, edited by R. E. Peterson (Texas Tech University, Lubbock, 1976), pp. 501–530.
[29] D. S. Nolan and B. F. Farrell, "The structure and dynamics of tornado-like vortices," J. Atmos. Sci. **56**, 2908 (1999).
[30] R. Fernandez-Feria, "Viscous and inviscid instabilities of non-parallel self-similar axisymmetric vortex cores," J. Fluid Mech. **323**, 339 (1996).
[31] V. Shtern and F. Hussain, "Hysteresis in a swirling jet as a model tornado," Phys. Fluids A **5**, 2183 (1993).